Hybrid PEO/sol-gel coatings loaded with Ce for corrosion protection of AA2024-T3

del Olmo, R.; López, E.; Matykina, E.; Tiringer, U.; Mol, J. M.C.; Mohedano, M.; Arrabal, R.

DOI
10.1016/j.porgcoat.2023.107667

Publication date
2023

Document Version
Final published version

Published in
Progress in Organic Coatings

Progress in Organic Coatings 182 (2023) 107667

Contents lists available at ScienceDirect

Progress in Organic Coatings

journal homepage: www.elsevier.com/locate/porgcoat

Hybrid PEO/sol-gel coatings loaded with Ce for corrosion protection of AA2024-T3

R. del Olmo [a,b,*,1], E. López [a,1], E. Matykina [a], U. Tiringer [c], J.M.C. Mol [c], M. Mohedano [a], R. Arrabal [a]

[a] Departamento de Ingeniería Química y de Materiales, Facultad de Ciencias Químicas, Universidad Complutense de Madrid, 28040 Madrid, Spain
[b] Department of Materials and Ceramics Engineering, CICECO Aveiro Institute of Materials, University of Aveiro, 3810-193 Aveiro, Portugal
[c] Delft University of Technology, Department of Materials Science and Engineering, Mekelweg 2, 2628 CD Delft, the Netherlands

ARTICLE INFO

Keywords:
PEO coating
Hybrid sol-gel coating
Green corrosion inhibitor
Active corrosion protection
Cerium

ABSTRACT

Plasma electrolytic oxidation (PEO) has been targeted as an eco-friendly alternative technology to conventional chromic acid anodizing (CAA) for corrosion protection of aluminium alloys in the aircraft industry. However, conventional PEO technology implies high energy consumption. Flash-PEO coatings (≤10 μm) produced in short treatment times (≤ 5 min) constitute a feasible way to overcome this limitation. Nevertheless, the long-term corrosion resistance is compromised, thus requiring novel sealing post-treatments. The present work studies the effect of stand-alone hybrid sol-gel (HSG) and Ce-doped hybrid sol-gel (HSG—Ce) coatings as a sealing post-treatment to evaluate the long-term corrosion resistance of Flash-PEO coatings on aluminium alloy (AA) 2024-T3. The characterization of the PEO, HSG, and HSG-Ce coatings was performed by scanning electron microscopy, X-ray diffraction, water contact angle, dry adhesion tests (ISO 2409), optical profilometry and Fourier transform infrared spectroscopy. The corrosion behaviour was assessed by electrochemical impedance spectroscopy up to 21 days (3.5 wt% NaCl). Active corrosion protection was assessed by immersion tests of artificially scratched coatings. Present findings reveal that low-energy-cost Flash-PEO coatings were successfully formed on AA2024-T3 alloy. Both HSG and HSG-Ce coatings were homogeneously formed on Flash PEO coating. Regarding the corrosion resistance, HSG-Ce showed significant scratch protection during 21 days of immersion in 3.5 wt% NaCl. The results suggest that, while the release of Si and Ce from the coating provided corrosion protection, NO_3^- release promoted localized corrosion phenomena in the scribe. This was associated with the preferential pitting corrosion phenomena at the Cu-rich intermetallic compounds instead of forming a thick and stable NO_3^--rich passive layer.

1. Introduction

One of the most widely used aluminium (Al) alloys in the aircraft industry is AA2024-T3 (e.g., fuselage, wing parts, and internal structures). This is owed to its low density, excellent formability, and, especially, its high strength-to-weight ratio [1]. However, the high complexity, heterogeneity and population density of intermetallic compounds in the AA2024-T3 microstructure have a detrimental effect on its corrosion resistance [2]. So far, the most common protection scheme for Al alloys in the aircraft industry is a multi-layer system: (i) a pre-treatment (a highly adherent oxide film formed by conventional anodizing), combined with (ii) multiple organic-based layers (polymer-based primer layers and paint). Both layers contain Cr(VI)-based compounds because of their excellent protection ability. However, they are highly toxic and carcinogenic, and their removal from wastewater is particularly costly [1,3].

Over the last decade, promising substitutes for chromic acid anodizing (CAA) have been identified, such as anodizing in tartaric-sulfuric acid (TSA) and boric-sulfuric acid (BSA) mixtures. The latter has been identified as toxic [4]. Both treatments are used for non-bonding and non-fatigue-sensitive applications, respectively. Nevertheless, none of these alternatives provides the same level of corrosion protection as

* Corresponding author at: Departamento de Ingeniería Química y de Materiales, Facultad de Ciencias Químicas, Universidad Complutense de Madrid, 28040 Madrid, Spain.
E-mail address: rubandom@ucm.es (R. del Olmo).
[1] These authors have equally contributed to the present work.

https://doi.org/10.1016/j.porgcoat.2023.107667
Received 22 December 2022; Received in revised form 4 May 2023; Accepted 9 May 2023
Available online 20 May 2023

CAA, which is still used in critical components [3,4]. Therefore, the search for high corrosion resistance Cr(VI)-free surface treatments with low thickness and compatible with sealing post-treatments is still of pivotal importance.

Depending on the application, Al cladding, commercial sol-gel, and Zr/Ti-based pre-treatments are used for corrosion protection of AA2024-T3 alloy [4]. However, critical structures are usually anodized for maximum corrosion protection and paint adhesion.

In this scenario, the lack of Cr-free alternatives is boosting the search for alternative surface treatments for anodizing, i.e., plasma electrolytic oxidation (PEO). PEO is a plasma-assisted electrochemical surface treatment characterized by anodizing in eco-friendly alkaline electrolytes at high voltages to produce ceramic coatings with a high level of corrosion protection on Al alloys [5]. Nevertheless, commercially, PEO technology does not compete with conventional anodizing due to its high energy consumption, i.e., high voltages (200–400 V), current densities (10–60 A dm^{-2}), and long treatment times (15–60 min) [5,6]. These conditions give rise to the formation of 50–200 μm-thick coatings, which strongly affect the fatigue properties, thus limiting their potential.

Therefore, to implement PEO technology as a feasible alternative to CAA, thin and short-time-application PEO coatings are required, i.e., Flash-PEO [7,8]. So far, several studies addressed the formation of Flash-PEO coatings on Al alloys with similar corrosion protection to conventional thick PEO coatings [7,9]. Nevertheless, the long-term corrosion resistance of such Flash-PEO coatings is comparable to that of the base material itself [7]. Future developments must include long-term corrosion protective sealing post-treatments [5].

Currently, most Cr-free sealing post-treatments originally developed for anodizing can be applied for PEO coatings, e.g., layered double hydroxides (LDH), organic polymeric coatings, silica-based coatings, etc. [10,11]. Among them, hybrid sol-gel (HSG) coatings stand out due to their overall improved corrosion and mechanical performance compared to conventional inorganic-based sol-gel coatings [12]. The formation of HSG coatings combines inorganic and organic polymerization. The inorganic part provides enhanced mechanical support, whereas the organic part adds flexibility and decreases treatment temperature [13,14].

This sealing post-treatment has been targeted as a corrosion-protective, cost-effective, simple, and eco-friendly strategy in several studies [15–17]. Although HSG coatings provide efficient barrier protection to Al alloys, they do not provide active corrosion protection when damage occurs. However, active corrosion protection is an important prerequisite to consider as aircraft components usually suffer damage during their service life.

To overcome this limitation, new formulations of HSG loaded with rare salt-based corrosion inhibitors (e.g., Ce(III), Li, molybdates, vanadates) have been investigated on bare AA2024-T3 and, more recently, on anodic films [18–21].

Among such inhibitors, the incorporation of Ce-based salts into the HSG formulation shows a remarkable improvement in the active corrosion protection properties. In detail, when corrosion occurs, Ce^{3+} ions are hydrolyzed, and insoluble Ce hydroxides precipitate on the cathodic sites on the AA2024-T3 surface. As a consequence, these compounds act as a protective barrier against oxygen diffusion and its reduction and hence lower the overall cathodic activity [19,22,23].

In this scenario, to the best of the author's knowledge, the available literature based on duplex PEO/HSG systems is non-existent for thin PEO coatings as the available studies are focused on developing conventional sol-gel coatings on thick PEO coatings (≥ 10 μm) [18,24,25].

The ultimate goal of the present work is to address this lack of understanding regarding the effect on corrosion resistance of a hybrid multilayer system based on HSG. Hereto, the present study aims to develop a multilayer protection scheme for legacy aerospace alloy AA2024-T3 by developing (i) a thin and cost-effective PEO coating (< 5 μm) and (ii) sealing post-treatments based on HGS and HGS—Ce.

2. Materials and methods

2.1. Surface preparation

The base material used in the present work is AA2024-T3, supplied by Famimetal S.L. (wt%: 3.8–4.9 Cu, 1.2–1.8 Mg, 0.3–0.9 Mn, <0.5 Fe, <0.5 Si, <0.25 Zn, <0.15 Ti, <0.10 Cr and Al balance). The size of the rectangular specimens was 40 mm × 25 mm × 2 mm. Prior to PEO treatment, all specimens were etched and desmutted following a commercial procedure recommended by Henkel and described in [7]. Once cleaned, the working area (~20 cm^2) was delimited using an epoxy resin (red stopping off laquer, MacDermid Enthone) with an electrical connection provided via a shielded copper wire for PEO treatment.

2.2. PEO coatings

The PEO treatments were performed using a 2 kW AC power supply (EAC-S2000, ET Systems Electronic). RMS (root mean square) voltage and current signals were recorded continuously using a Keithley KUSB-3116 data acquisition card (500 kS/s). The experimental setup was equipped with a cylindrical counter electrode (AISI 316L) with a 2 L jacketed cell operating at constant temperature (20 ± 1 °C) under continuous stirring of the electrolyte. The electrolyte composition and the PEO electrical parameters are summarized in Table 1.

After the PEO process, all samples were cleaned in deionized water, isopropanol and dried with hot air steam. The specific energy consumption (P_{tot}) was calculated by integrating the voltage-current signals over time.

2.3. Hybrid sol-gel preparation

Two HSG coatings were applied onto the PEO-coated AA2024-T3 alloy. The first one was synthesized without corrosion inhibitor and used as a reference. The second was doped with $Ce(NO_3)_3{\cdot}6H_2O$.

Both HSG coatings are GPTMS-TEOS-based (3-(glycidyloxypropyl) trimethoxy silane and tetraethoxysilane, respectively). To enhance the resultant barrier properties, coating thickness and density of the GPTMS-TEOS-based coating, SiO_2 nanoparticles were added to the GPTMS/TEOS solution [26,27]. Namely, the HSG synthesis was performed according to the experimental procedure detailed in [22,23]. The molar ratios of the hybrid sol-gel coatings were TEOS/GPTMS/SiO2 = 0.5/0.5/0.54 and TEOS/GPTMS/SiO2/Ce = 0.5/0.5/0.54/0.03, for HSG and HSG—Ce, respectively.

Both coatings were deposited by using the dip-coating technique with a withdrawal rate of 30 cm min^{-1}. The dwell time in the solution was 1 s. Samples were heat-treated for 1 h at 120 °C to complete the polymerization between the sol and the PEO-coated substrate.

The designation of the studied coatings is PEO, HSG (inhibitor-free), and HSG-Ce (Ce-doped HSG coating). Note that all the specimens

Table 1
PEO electrolyte and applied conditions.

Electrolyte	Voltage (V^+/V^-) [V]	Voltage initial ramp [s]	Frequency [Hz]	Limiting current [mA cm^{-2}]	Time [s]
10.5 g L^{-1} $Na_2O(SiO_2)_3{\cdot}5H_2O$ (CAS: 13729) 5 g L^{-1} $Na_3(PO_4){\cdot}12H_2O$ (CAS: 10101–89-0) 2.8 g L^{-1} KOH (CAS: 1310-58-3)	490/−110 (square signal)	60	400	100	100

include a PEO layer. For ease of understanding, Fig. 1 summarizes the multi-layer protection scheme addressed in the present work.

2.4. Coating characterization

The studied coatings were analyzed in the top and cross-sectional views (mechanically ground through successive grades of SiC paper and polished with a 1 μm diamond paste), using a JEOL JSM 6400 scanning electron microscope (SEM) equipped with energy dispersive X-ray microanalysis (EDS) equipment for semi-quantitative analysis (Oxford Link).

The thickness of the studied coatings was determined using an ISOSCOPE FMP10 eddy current meter (Fischer) equipped with an FTA3.3H probe. ImageJ software was used for image analysis of the PEO coating porosity, using at least three SEM plan view micrographs at ×500 magnification for each coating.

Identification of the crystalline phases in the PEO coating was carried out by X-ray diffraction (XRD) analysis using a Philips X'Pert-MPD instrument (Cu Kα = 1.54056 Å). XRD patterns were analyzed with the ICDD™ database. XRD spectra using grazing incidence (0.5°) were acquired in the 2θ range from 20° to 80° with a step size of 0.05° and a dwell time of 2 s per step.

Deionized water contact angle (WCA) measurements were carried out using an FTA 1000/FTA instrument and FTA32 software. The values quoted are the average of 6 drops measured on two samples (3 drops each).

Dry adhesion was evaluated in triplicate on HSG-coated specimens following the ISO 2409 standard. The rating system is based on the detached surface area (%) after the test (rating 0: no detachment; rating 5: complete detachment).

Real and topographic 3D images were obtained with an InfiniteFocusSL optical profilometer (InfiniteFocusSL, Alicona). High-resolution 3D measurements were carried out using a motorized stage and ×10 and ×50 magnification objectives. The topographic information was analyzed with the IF-Measure Suite software to extract roughness parameters, such as S_a (the difference in height of each point compared to the arithmetic mean of the surface) and S_{10z} (the sum of the arithmetic means of the five highest peaks and the five deepest valleys). Given that HSG coating layers are transparent, these were carbon-coated to ascertain the abovementioned roughness parameters.

Fourier transform infrared spectroscopy (FTIR) analysis was performed using a Nicolet iS50 instrument equipped with a KBr beam splitter, a DTSG-KBr detector, and a SpectraTech Performer ATR accessory with a diamond crystal. The spectrum obtained by the FTIR technique is in the mid-IR region (4000 and 500 cm^{-1}). The resolution and number of scans were set at 0.5 cm^{-1} and 7500, respectively.

2.5. Corrosion evaluation

2.5.1. Electrochemical impedance spectroscopy

The corrosion resistance of PEO, HSG, and HSG-Ce coatings was evaluated by electrochemical impedance spectroscopy (EIS) in 3.5 wt% NaCl aqueous solution at room temperature. A GillAC potentiostat (ACM Instruments) connected to an electrochemical cell with a Ag/AgCl reference electrode (3 M KCl), a graphite rod auxiliary counter electrode, and the working electrode (~ 1 cm^2) AA2024-T3 were used. All measurements were performed inside a Faraday cage (Gamry Instruments VistaShield™) to enable reproducibility of the measurements by limiting any effects of possible external interference. In all tests, a sine wave of 10 mV amplitude and a frequency range of 10^5–10^{-2} Hz was applied at different immersion times (1 h, 3, 7, 14, and 21 days). The Zview™ software was used for the EIS data analysis. The goodness of fit was guaranteed by chi-square values <0.01 (square of the standard deviation between the original data and the calculated spectrum) and, additionally, by weighted sum of squares <1.0. The latter is proportional to the average percentage error between the data points and the fitting points. All measurements were repeated twice.

2.5.2. Active corrosion protection evaluation

Immersion tests of PEO, HSG, and HSG-Ce coatings were performed on scratched samples. An artificial cross-shaped defect was created with a knife blade; the defect depth was higher than the thickness of the coating. Scratched coatings were monitored by optical microscopy and SEM/EDS analysis after 1, 3, 11, and 21 days of immersion in a 3.5 wt% NaCl aqueous solution. After the tests, the active corrosion protection was evaluated by SEM/EDS analysis.

3. Results and discussion

3.1. PEO coating formation and characterization

Fig. 2 shows the voltage- and current density-time transients during the PEO treatment of the 2024-T3 alloy. As can be seen, the voltage ramp (first 60s) is accompanied by an increase of the current (~ 100 mA cm^{-2}). There is a current maximum at ~5 s which is related to several phenomena such as the thinning of the barrier layer and dissolution of intermetallic compounds [11]. After ~45–55 s (~ 180–250 V), numerous electrical discharges on the surface were observed which produced instantaneous current oscillations [6,8]. At this stage, there is also significant gas evolution (oxygen in the positive and hydrogen in the negative pulses due to oxidation and reduction of water, respectively [28]).

Note that the energy consumption value (~ 5.3 kW h m^{-2} μm^{-1}) and

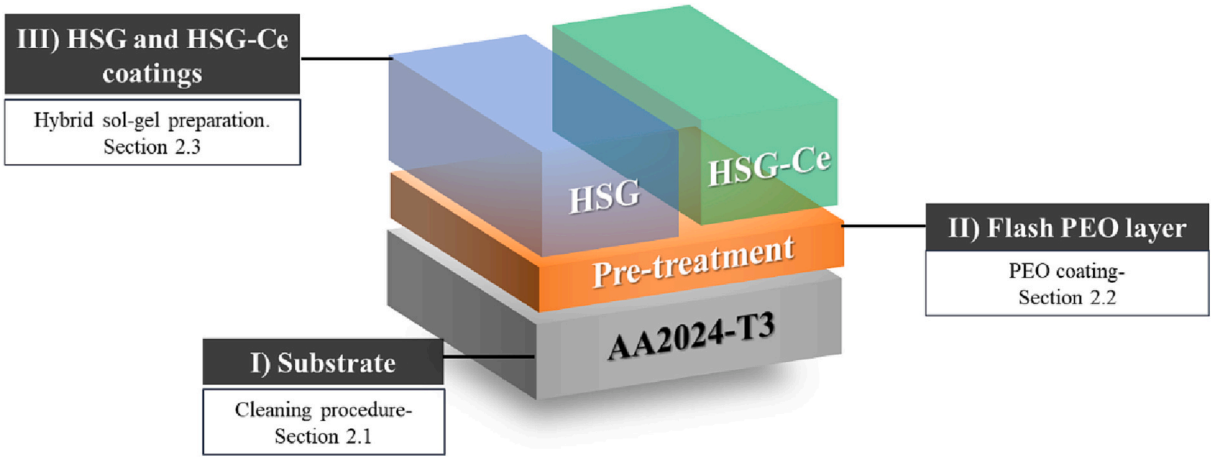

Fig. 1. Schematic representation of the multi-layer corrosion protection scheme addressed in this study for AA2024-T3.

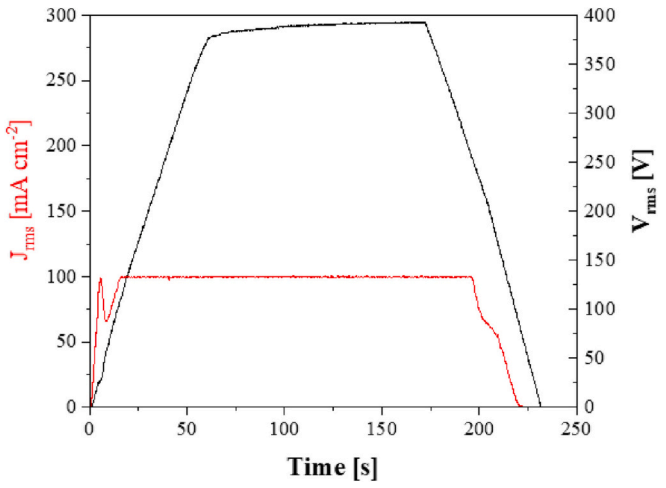

Fig. 2. Voltage- and current density-time responses during Flash-PEO treatment of AA2024-T3.

coating thickness (2.5 ± 0.3 μm) are much lower than those for the conventional thick PEO coating for Al alloys, i.e., 20–27 kW h m^{-2} μm^{-1} and 50–150 μm, respectively [5].

Notwithstanding, the energy consumption value is higher than that reported in the literature for other thin PEO coatings (~ 2–2.5 μm) developed in silicate (2.2 kW h m^{-2} μm^{-1}) [8,29] and phosphate electrolytes (1.3–4.7 kW h m^{-2} μm^{-1}) on AA2024-T3 [6].

On that basis, although the coating growth rate of the studied PEO coating (0.7 μm min^{-1}) is in line with the reported coating growth rates for silicate- (0.4–1.3 μm min^{-1}) [8,29] and phosphate-based electrolytes (1.3–3.5 μm min^{-1}) [30,31], the slightly higher energy consumption reported in the present work may be associated with the AC PEO processing regime mode. The negative pulse involved in the AC regime is not intended for the PEO coating formation, thus making the process less energy efficient than the DC regime [6,11].

XRD analysis reveals the presence of γ-Al_2O_3 (ICDD reference pattern 00-010-0425) in the studied PEO coating. The detection of Al (ICDD reference pattern 00-004-0787) is due to the low coating thickness, thereby allowing the interaction of X-rays with the base material (Fig. 3).

Note that the α-Al_2O_3 phase, which is typically found in conventional

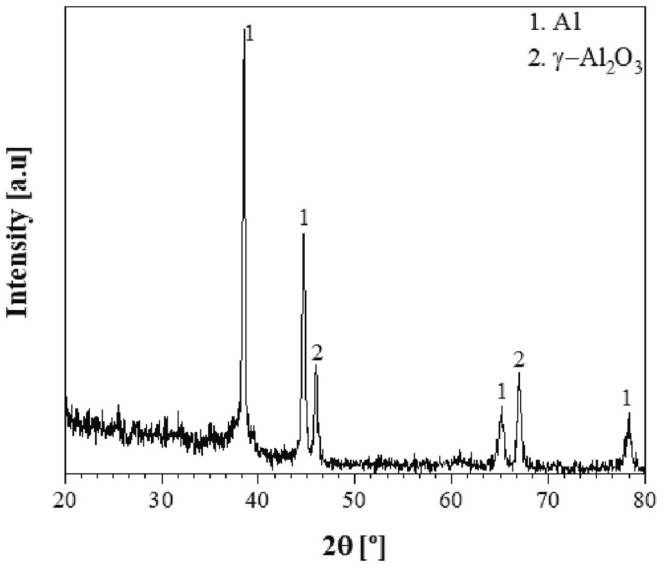

Fig. 3. XRD pattern of the studied PEO coating upon application on AA2024-T3.

thick PEO coatings (>20 μm) [11], is not detected in the present study. The predominance of metastable γ-Al_2O_3 over the stable α-Al_2O_3 phase is to be expected since the short treatment time of PEO involves short-lived microdischarges and low coating thickness and, therefore, higher cooling rates in the discharge channels after they are extinguished (i.e. heat dissipation towards the substrate and electrolyte is easier for thin coatings) [7,8].

3.2. PEO and HSG coatings characterization

Fig. 4 shows the top view scanning electron micrographs of the PEO, HSG, and HSG-Ce coatings.

The short-lasting discharges of the PEO process result in a homogeneous surface coating morphology (Figs. 4a) with very sparse submicrometric and circular-like pores (Figs. 4b). Several authors reported that this circular shape is associated with the prompt solidification of the coating material after the discharge event [5,11]. It is worth mentioning that the pore size in the PEO coating is in the order of a few hundred nanometres (~225 ± 110 nm), which may be explained by the short duration of the treatment. Another explanation may be even related to the AC mode as the DC regime promotes the formation of larger pores in phosphate- (~3 μm^2) [7] and silicate-based (~5–7 μm^2) [9,32] electrolytes on AA2024-T3.

The studied HSG and HSG-Ce coatings showed a smooth and homogeneous morphology (Fig. 4 c-f). In both cases, no surface cracks or detachment areas were observed (Fig. 4 c, e). Notwithstanding, the surface morphology of the PEO layer is evident for HSG coating (Fig. 4 c, d).

In the case of HSG-Ce coating, no PEO pre-treatment layer was visible (Fig. 4 e, f). This is due to the beneficial effect of Ce^{3+} cations, which promote the condensation and polymerization of the inorganic and organic networks in the HSG formulation [19,27].

As shown in Table 2, EDS analysis of the PEO coating indicates the presence of O and Al as the main constituent elements and a small contribution of Si and P that were incorporated from the electrolyte. The detection of Cu is probably associated with the penetration of the electron beam beyond the coating thickness since it is one of the main elements in AA2024-T3.

By contrast, EDS analyses of HSG and HSG-Ce coatings reveal higher O, Si, and C concentrations than the PEO coating. This is due to the use of TEOS and GPTMS in the sol-gel formulation. Note that the C content obtained by EDS analysis is less accurate as it is an element of relatively low atomic number (in the PEO coating, C is associated with surface contamination).

The surface of HSG coating reveals some randomly distributed bright deposits with higher concentrations of Al and P and lower contents of Si and C (marked as 2 in Fig. 4d). These deposits were detected in thinner areas on the HSG coating.

Note that Ce was relatively homogeneously distributed for the HSG-Ce coating (0.2 at.%; marked as 1 in Fig. 4e). This finding is opposite to the results of an author's previous work [22], where Ce could not be detected in a Ce-doped HSG coating formed on an anodized AA2024-T3. The authors associated this phenomenon with the possible precipitation of Ce-containing nanoparticles within the inner coating part. By contrast, Tiringer et al. [23], reported a homogeneous Ce distribution in higher concentration (0.6–0.9 at.%) on an HSG-Ce coated AA7075-T6.

The results regarding the Ce detection/distribution can be inferred to be related to the possibly different interaction between the PEO layer (e.g., morphology, chemical composition, etc.) and the Ce-containing HSG formulation during the curing process in comparison to prior works.

To accurately address the distribution of the different elements through the coating structure, including Ce, cross-sectional view SEM analysis of the studied coatings is depicted in Fig. 5. EDS analysis is summarized in Table 3.

Cross-sectional micrographs of the PEO coating revealed a multi-layered structure, with dense and porous band sublayers of ~2.5 ±

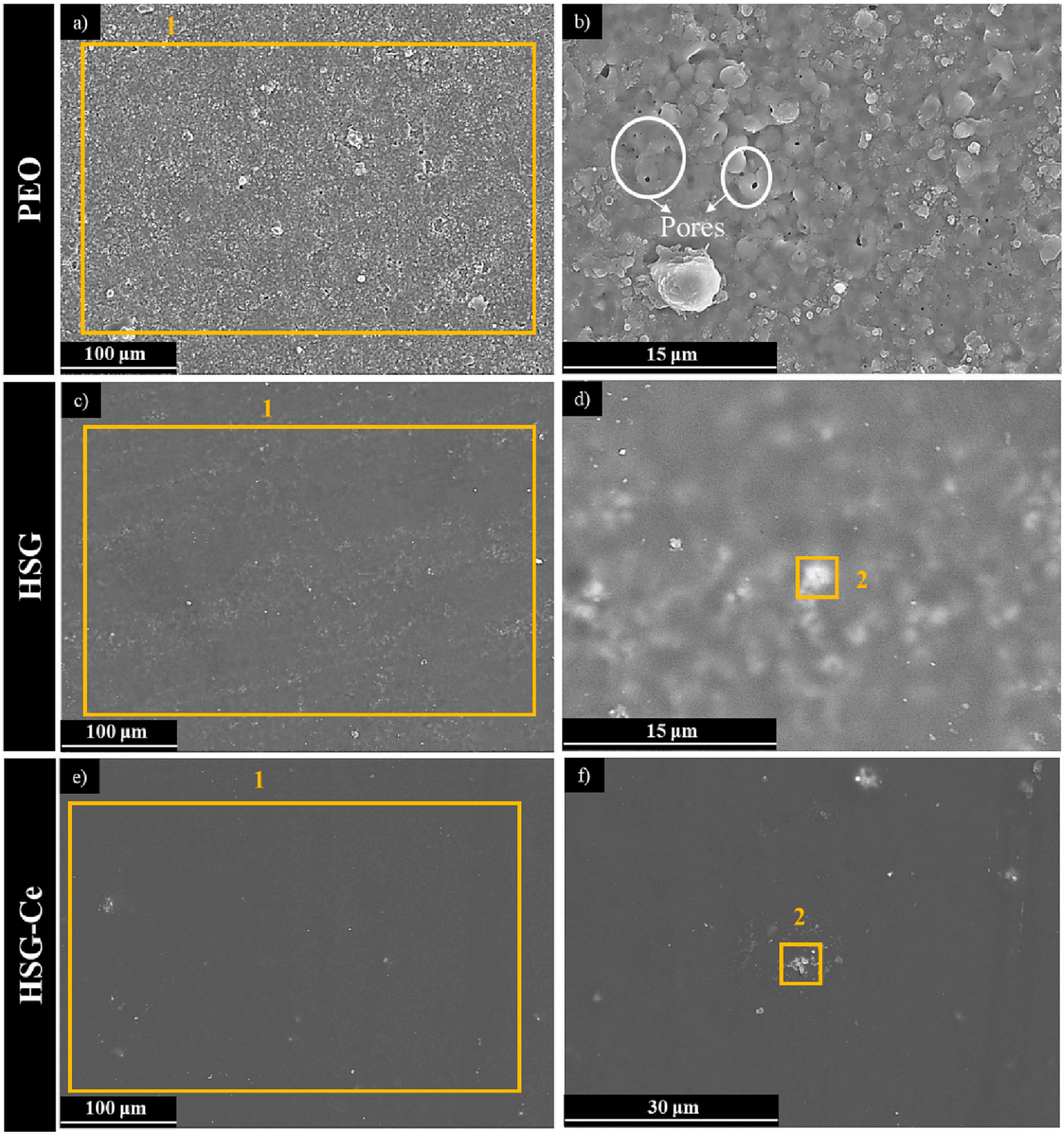

Fig. 4. Plan view secondary electron images of the PEO (a, b), HSG (c, d), and HSG-Ce (e, f) coatings. EDS analysis results of the yellow boxed areas are presented in Table 2. (For interpretation of the references to colour in this figure legend, the reader is referred to the web version of this article.)

Table 2
EDS analysis (at.%) of PEO, HSG, and HSG-Ce coatings. Locations are denoted on the top-view SEM micrographs in Fig. 4.

Coating	Location	O	Al	Si	P	C	Ce	Cu
PEO	1	49.1	32.5	1.3	0.5	16.2	–	0.4
HSG	1	37.7	8.6	14.0	0.1	39.4	–	0.2
	2	48.8	24.8	3.8	0.4	22.1	–	0.1
HSG-Ce	1	42.8	1.9	15.6	–	39.5	0.2	–

0.3 µm thickness (Fig. 5a). The pore band and microcracks may be caused by the evolution of gas bubbles (mainly O_2 and H_2) entrapped during the rapid solidification of molten material in the discharge channels during the PEO process [5,11].

The application of HSG and HSG-Ce sealing post-treatments gives rise to the formation of homogeneous films over the PEO coating with comparable thickness values ($\sim 4.0 \pm 0.4$ µm) (Fig. 5 c-f).

The EDS analysis reveals that the PEO coating consists mainly of Al, O, and a low Si content. In addition, a higher percentage of Al, Mg, and P is detected in the inner areas of the coating. Al and Mg stem from the substrate, while P and Si originate from the PO_4^{3-} and SiO_3^{2-} anions from the electrolyte, respectively. These anions migrate towards the substrate

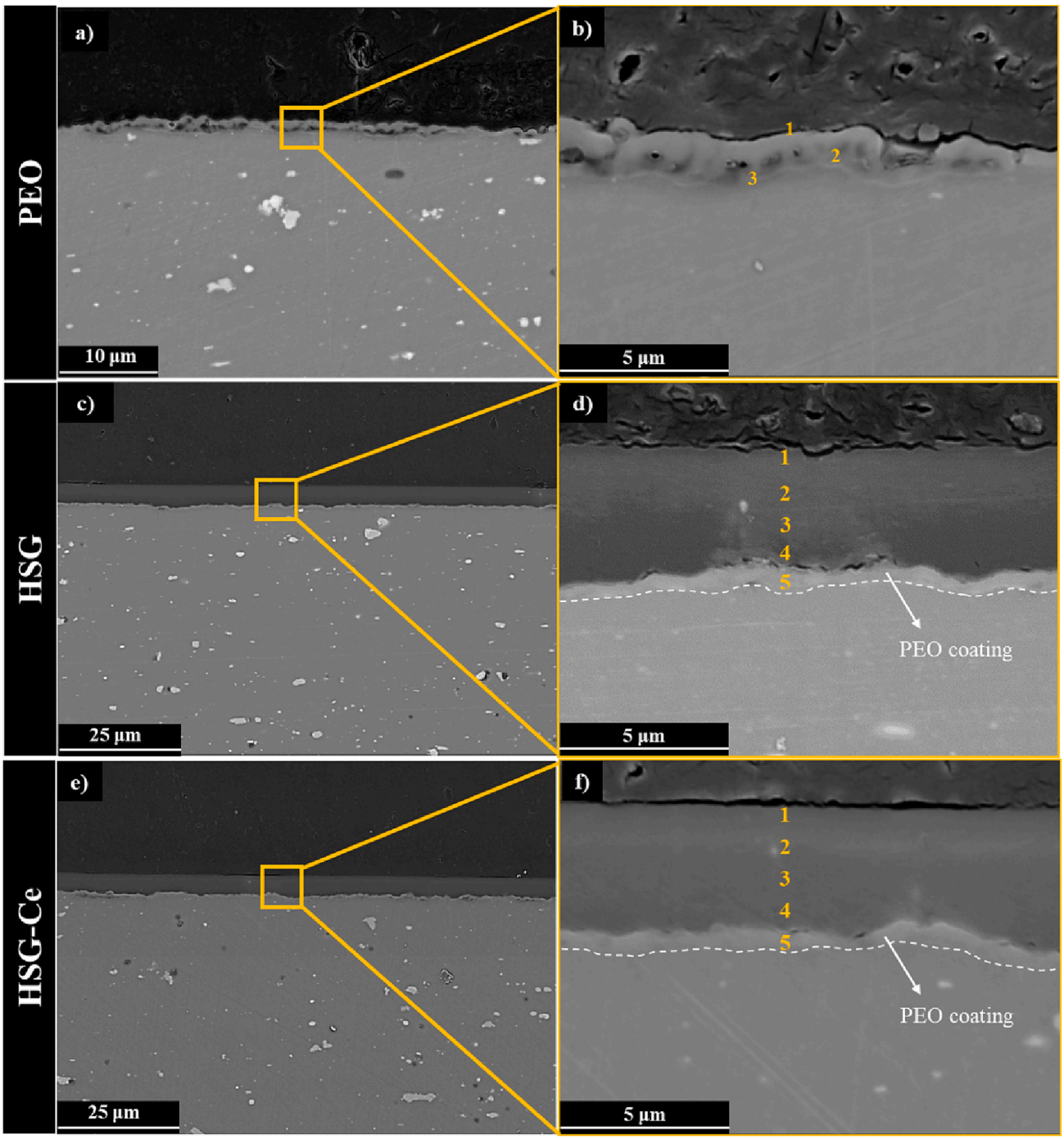

Fig. 5. Cross-section secondary electron images of the PEO (a, b), HSG (c, d), and HSG-Ce (e, f) coatings. EDS analysis results of the yellow boxed areas are presented in Table 3. (For interpretation of the references to colour in this figure legend, the reader is referred to the web version of this article.)

during the positive pulses during the PEO process [31,33].

The EDS analysis of the HSG and HSG-Ce coatings confirms a noticeable Al incorporation in the inner sol-gel structure (Table 3). Al incorporation is usually associated with the interaction between the bare Al alloy [34,35] or anodic layer [16,22] and the HSG formulation.

In the present study, the presence of Al in the HSG coating is related to the dissolution of the Al oxides from the Flash-PEO coating during HSG deposition [36,37]. Namely, the low stability of Al_2O_3 in the acidic HSG formulation (pH ~ 6) and the applied temperature during the curing stage (~120 °C) may explain the Al diffusion phenomenon within the HSG coating [37]. This may also confirm the PEO coating thinning (Fig. 5a) after the HSG deposition (Fig. 5 d,f), i.e., from 2.5 ± 0.3 to 1.3 ± 0.3 µm.

Another observation is the lower porosity of the PEO layer in the HSG and HSG-Ce coatings compared to the non-sealed PEO coating (Fig. 5 a, b). This partial pore sealing may be associated with the penetration of HSG through the PEO coating c. Variations in silicon content may be associated with the different distribution of SiO_2 particles in the HSG coating (marked as 1–3 in Fig. 5d, f).

To ascertain the HSG adhesion on the PEO coating, a further qualitative dry adhesion test was performed on the studied HSG and HSG-Ce coatings (ISO 2409). The results revealed a rating of 0 for both HSG and HSG-Ce coatings, thus confirming excellent interaction between the PEO layer and the HSG (Fig. S1).

Table 3
Cross-section EDS analysis (at.%) of PEO, HSG, and HSG-Ce coatings. Locations are denoted on the cross-view SEM micrographs in Fig. 5.

Coating	Location	O	Al	Si	P	C	Cu	Mg	Ce
PEO	1	39.7	15.7	0.9	–	43.4	0.1	0.2	–
	2	36.6	37.3	0.9	–	24.6	0.3	0.3	–
	3	22.1	49.2	0.5	2.3	24.6	0.8	0.5	–
HSG	1	22.5	–	11.0	–	66.4	0.1	–	–
	2	27.4	0.4	32.5	–	39.5	0.2	–	–
	3	36.9	4.6	17.5	–	40.9	0.1	–	–
	4	46.5	23.2	5.8	–	24.0	0.2	0.3	–
	5	30.2	41.4	4.0	–	23.0	0.8	0.6	–
HSG-Ce	1	28.4	–	10.4	–	61.0	0.1	–	0.1
	2	24.6	0.3	31.1	–	43.2	0.3	–	0.5
	3	31.4	1.6	23.0	–	43.2	0.3	–	0.5
	4	37.8	11.9	12.6	–	37.2	0.2	0.1	0.2
	5	39.7	30.9	2.6	–	25.9	0.5	0.4	–

Regarding the Ce distribution in the HSG-Ce coating, cross-section EDS analysis confirms the heterogeneous distribution of Ce across the coating thickness. Ce concentration was higher (0.5 at.%; marked as 2–3 in Fig. 5f) in the middle-upper region (~ 1.5 μm from the surface) than that in the inner coating part (0.2 % at.; marked as 4 in Fig. 5f). According to U. Tiringer et al. [23,27], this may be associated with the precipitation of Ce-containing nanoparticles within the coating structure, especially during the HSG curing step. Fig. 6 shows the FTIR spectra for the PEO, HSG, and HSG-Ce coatings.

PEO coating (Fig. 6) shows a low-intensity signal at 2871 cm^{-1} and a broad band below 960 cm^{-1}. These bands correspond to C—H bond stress vibrations (surface contamination) and the vibrational modes of the γ-Al_2O_3 (as detected in the XRD pattern; Fig. 3) [38], respectively.

Both HSG and HSG-Ce coatings showed similar bond vibrations at 3100–3600 cm^{-1} and 1633 cm^{-1} assigned to the O—H bonds (water molecules) and Si-OH groups from the HSG formulation [39]. The C—H bond vibrations at 2937–2871 cm^{-1} are mainly associated with the GPTMS precursor (-CH_3 and -CH_2 groups) and contamination [19,39]. Signals corresponding to Si-O-Si bonds appear at 960–1260, 785, 545, and 440 cm^{-1} [40]. The most intense bands correspond to asymmetric vibrations around 1030 cm^{-1} and are an indication of the complete formation of the sol-gel coating [40,41].

FTIR spectra of HSG-Ce coating compared to HSG show a lower signal intensity of the Si-O-Si bands and the asymmetric vibration of the epoxy ring (at 910 cm^{-1}). Several authors suggest that Ce^{3+} cations in the HSG formulation promote the catalytic epoxy ring opening by the exothermic reaction produced by nitric acid catalyst during sol-gel preparation [23,27]. This favors the organic precursor (GPTMS) cross-linking over the inorganic component (TEOS). Note that a higher concentration of Ce (>0.1 M) in the HSG formulation (GPTMS-TEOS) may promote (i) the destabilization of the Si-O-Si network and (ii) the formation of pores over the HSG coating surface [34,35]. Present findings reveal that the used concentration (0.03 M) is in the range to promote the formation of a stable and pore-free HSG-Ce coating over the Flash PEO coating surface (Figs. 4e, f). To further correlate the effect of HSG sealings on the topographic properties of the PEO coating, Fig. 7 shows the 3D topographic maps and WCA values of the studied coatings.

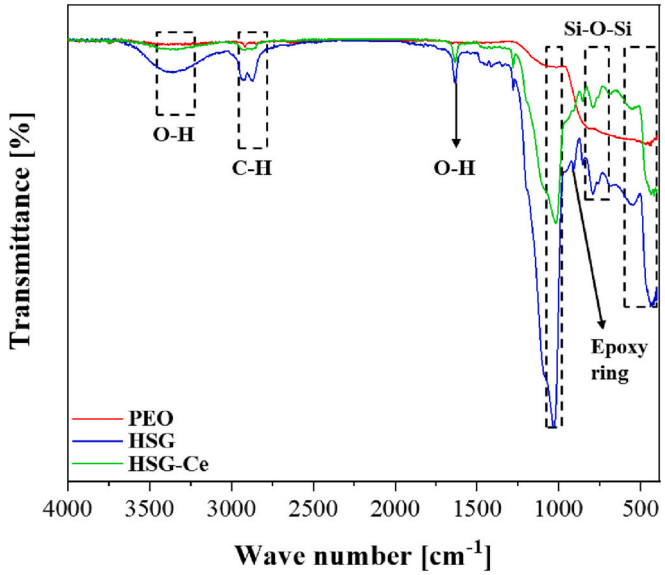

Fig. 6. FTIR spectra of PEO, HSG, and HSG-Ce coatings.

As can be seen in 3D topographical maps, all studied coatings show parallel bands and small circular depressions from the base material topography (Fig. 7a). The presence of these bands is due to the rolling process typical in the manufacturing of AA2024-T3 wrought substrate. The concavities correspond to the dissolution of intermetallic compounds after the chemical cleaning (see Section 2.1).

Note that, although no significant topographic differences in S_a and S_{10z} values were observed on the 3D maps, the inherent porosity and topographical heterogeneities of the PEO coating result in rougher surfaces than HSG-coated samples (Table 4). This may be related to the homogeneous HSG deposition on the PEO layer since the increase of roughness values in HSG coatings is usually associated with the presence of heterogeneities over the surface [23,42].

Regarding the WCA values (Fig. 7b), the PEO coating shows relatively high hydrophilicity with a contact angle value of (51 ± 7)°. This is due to the presence of sub-micrometric pores and heterogeneities on the PEO coating surface [7]. On the other hand, the non-porous nature and homogeneous distribution of HSG and HSG-Ce coatings over the PEO coating surface result in higher contact angle values [35], namely, (101 ± 6)° and (94 ± 4)° for HSG and HSG-Ce coatings, respectively.

Note that the presence of cerium in HSG coating decreases its hydrophobicity. A similar effect was observed by Hernández-Barrios et al. [41]. The authors reported that the catalytic opening of the epoxy ring (GPTMS) after Ce incorporation results in the formation of additional hydrophilic O—H bonds on the HSG coating surface, which corroborates with the FTIR analysis (Fig. 6).

3.3. Corrosion evaluation of PEO and HSG coatings

Fig. 8 shows the Bode plots obtained for the PEO, HSG, and HSG-Ce specimens after 1 h and 21 days of immersion in a 3.5 wt% NaCl aqueous solution (bare AA2024-T3 was also included as reference). For further information, Fig. S2 shows the impedance at low frequency (10 mHz) $|Z|_{10\ mHz}$ of the studied coatings at different immersion times.

The Bode plots of studied specimens show the presence of three distinct regions: (i) the high-frequency range (10^3–10^5 Hz), related to the response of the outer coating part at the HSG coating/electrolyte interface, (ii) the intermediate frequency range (10^0–10^3 Hz), related to the HSG interlayer, and (iii) the low-frequency range (10^{-2}-10^0 Hz),

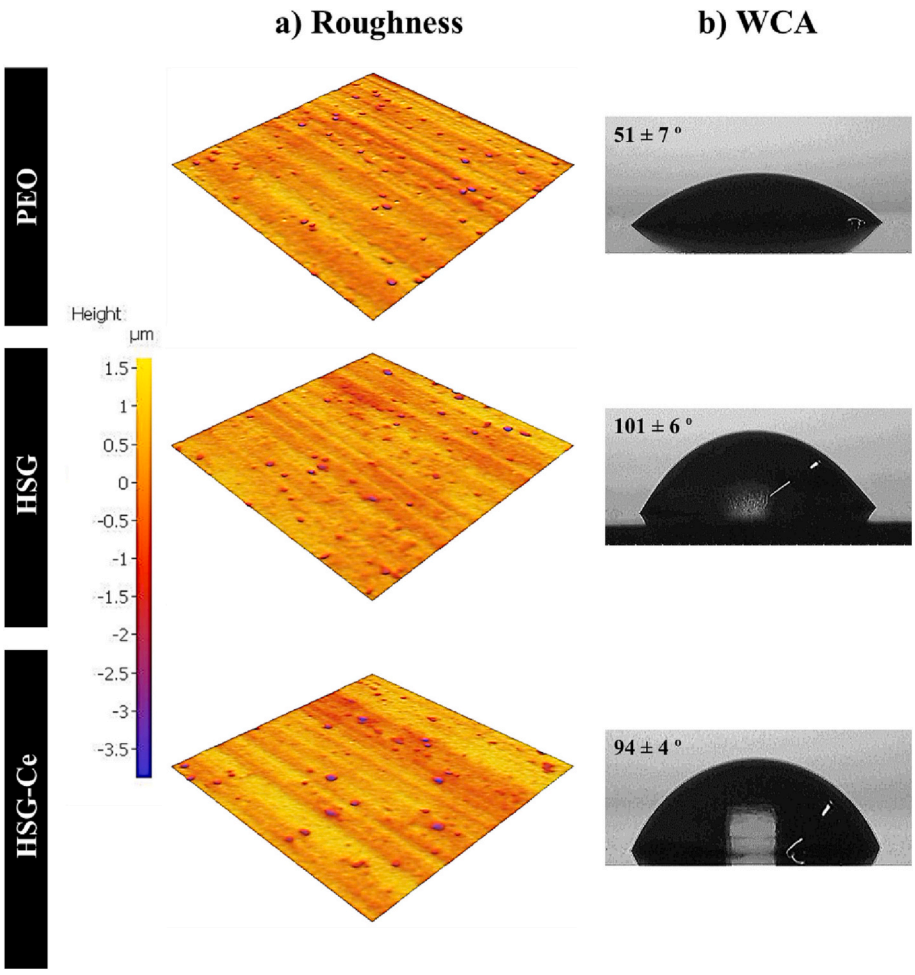

Fig. 7. (a) Optical 3D-topographical maps and (b) WCA images of the PEO, HSG, and HSG-Ce coatings.

Table 4
Roughness values of studied PEO, HSG, and HSG-Ce coatings on the 2024-T3 alloy.

Coating	S_a (µm)	S_{10z} (µm)
PEO	0.31 ± 0.03	6.2 ± 2.0
HSG	0.26 ± 0.01	3.8 ± 0.3
HSG-Ce	0.29 ± 0.01	3.4 ± 0.3

related to the charge transfer processes at the inner metal/PEO barrier layer interface. The latter is well-known to provide an estimation of the overall corrosion resistance, where higher values of $|Z|_{10\ mHz}$ indicate a lower corrosion rate [11,43].

For a short immersion time (1 h), the impedance modulus values of the PEO and HSG-coated specimens (Fig. 8a) were similar and two orders of magnitude higher than that for the reference bare AA2024-T3, denoting a corrosion resistance improvement. Despite this, both PEO and HSG coatings revealed the presence of an impedance drop in the low-frequency range. This phenomenon is commonly associated with electrolyte penetration through the coating layers [42,44]. This impedance drop was not detected in the HSG-Ce coating, which, in turn, showed the highest impedance modulus values among the studied coatings.

Regarding the phase angle-frequency plots (Fig. 8b), both HSG and HSG-Ce coatings show a phase angle drop in the mid-high frequency range, thus indicating diffusion phenomena of corrosive species throughout the HSG layers [22,45]. By contrast, the PEO coating shows a superior response of the outer (10^3–10^5 Hz) and the inner barrier (10^0–10^{-2} Hz) layers compared to HSG-coated specimens. This higher stability is also in line with the similar impedance modulus of the PEO coating compared to HSG-coated specimens.

For longer immersion times (21 days), the PEO coating shows a two magnitude orders decrease in the impedance modulus over the entire frequency range. Namely, the impedance modulus of the PEO coating decreased after 3 days of immersion (Fig. S2) and, after 21 days of immersion was comparable to the reference AA2024-T3 alloy (Fig. 8c). By contrast, HSG-coated specimens show a minimal decrease in the impedance moduli at all the studied immersion times (Fig. S2), indicating the beneficial effect of the HSG coating on long-term corrosion resistance (Fig. 8b).

The phase angle values at high frequency were higher for HSG and HSG-Ce coatings compared to those for PEO coating (Fig. 8d). However, at low frequencies, the phase angle values of PEO, HSG and HSG-Ce coatings were higher than those for 1 h of immersion. This may be attributed higher protective character of the HSG layer and/or the protective character of corrosion products from the underneath PEO layer [17,36].

The equivalent circuits used to interpret the EIS results are represented in Fig. 9. Considering the non-ideal behaviour (non-ideal resistor) of the system, constant phase elements (CPE) were used.

For the PEO coating at short immersion times (Fig. 9a), the equivalent circuit elements include R_s (solution resistance), CPE-p/R_p (capacitive and resistive behaviour of the outer porous layer), and CPE-b/R_b (capacitive and resistive behaviour of the inner layer).

After 21 days of immersion (Fig. 9b), the outer and inner PEO coating layers behave as a single oxide layer, giving an overall response of (CPE-

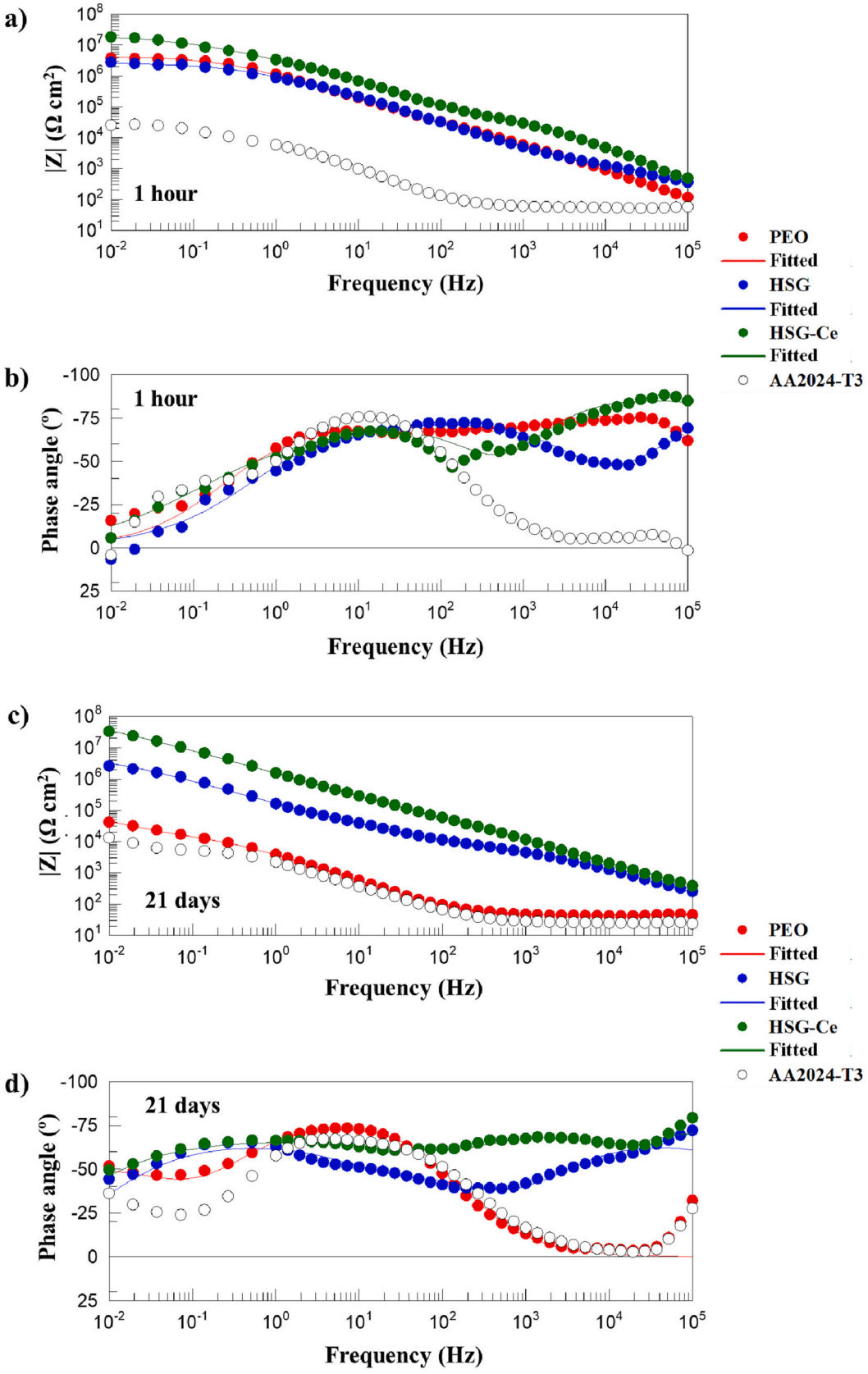

Fig. 8. Impedance- and Phase angle-frequency plots of all studied coatings after (a, b) 1 h and (c, d) 21 days of immersion in 3.5 wt% NaCl (aq.) solution. Plotted data by Zview software correspond to the most representative specimen of two replicas.

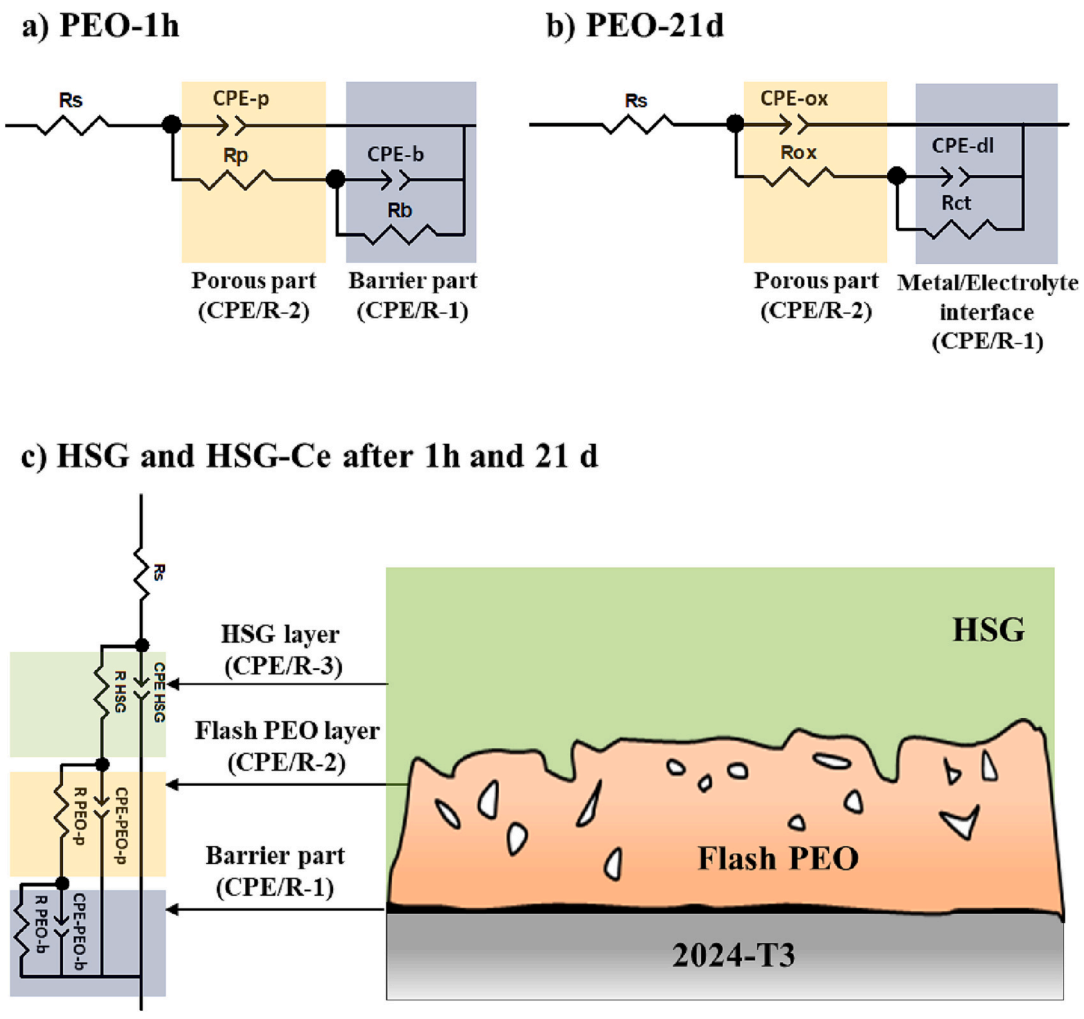

Fig. 9. Equivalent circuits to fit the experimental EIS data for (a, b) PEO, and c) HSG and HSG-Ce coatings after 1 h and 21 d of immersion in 0.1 mol L^{-1} NaCl solution.

ox/R_{ox}) at medium frequencies. The time constant at low frequencies is defined by the charge transfer resistance (R_{ct}) and the capacitive behaviour of the double layer at the metal/electrolyte interface (CPE-dl).

In the case of the HSG and HSG-Ce coatings (Fig. 9c) at the studied immersion times, the equivalent circuit elements include the stand-alone sol-gel layer (CPE-HSG/RHSG) response, the outer layer of the PEO coating response (CPE-PEO-p/R PEO-p) and, the contribution of the inner layer of the PEO coating (CPE-PEO-b/R PEO-b).

Table 5 shows the electrical parameters obtained by fitting the equivalent circuits for 1 h and 21 days.

For easier understanding, the simulation parameters corresponding with the different coating parts detailed in Fig. 9, will be named as follows:

Table 5
Fitted electrical parameters of studied coatings after 1 h and 21 days of immersion in 3.5 wt% NaCl solution.

Coating	CPE-1	n-1	R-1	CPE-2	n-2	R-2	CPE-3	n-3	R-3
1 h									
PEO	$1.5{\cdot}10^{-7}$ ($\pm5{\cdot}10^{-8}$)	0.73 ($\pm$0.01)	$4.2{\cdot}10^{6}$ ($\pm7{\cdot}10^{5}$)	$5.2{\cdot}10^{-8}$ ($\pm$ $2{\cdot}10^{-9}$)	0.90 ($\pm$0.01)	$1.70{\cdot}10^{4}$ ($\pm4{\cdot}10^{3}$)	–	–	–
HSG	$1.7{\cdot}10^{-7}$ ($\pm3{\cdot}10^{-8}$)	0.48 ($\pm$0.09)	$2.8{\cdot}10^{6}$ ($\pm3{\cdot}10^{5}$)	$8.5{\cdot}10^{-8}$ ($\pm$ $6{\cdot}10^{-9}$)	0.86 ($\pm$0.03)	$5.0{\cdot}10^{4}$ ($\pm1{\cdot}10^{3}$)	$2.3{\cdot}10^{-8}$ ($\pm2{\cdot}10^{-9}$)	0.88 ($\pm$0.04)	$1.66{\cdot}10^{4}$ ($\pm2{\cdot}10^{3}$)
HSG-Ce	$6.3{\cdot}10^{-8}$ ($\pm8{\cdot}10^{-9}$)	0.53 ($\pm$0.03)	$2.1{\cdot}10^{7}$ ($\pm2{\cdot}10^{6}$)	$2.6{\cdot}10^{-8}$ ($\pm$ $5{\cdot}10^{-9}$)	0.88 ($\pm$0.02)	$8.2{\cdot}10^{5}$ ($\pm2{\cdot}10^{4}$)	$4.6{\cdot}10^{-9}$ ($\pm1{\cdot}10^{-10}$)	0.98 ($\pm$0.01)	$5.4{\cdot}10^{4}$ ($\pm3{\cdot}10^{3}$)
21 days									
PEO	$1.6{\cdot}10^{-4}$ ($\pm4{\cdot}10^{-5}$)	0.73 ($\pm$0.07)	$2.5{\cdot}10^{5}$ ($\pm2{\cdot}10^{4}$)	$5.0{\cdot}10^{-5}$ ($\pm8{\cdot}10^{-6}$)	0.87 ($\pm$0.01)	$1.6{\cdot}10^{4}$ ($\pm4{\cdot}10^{3}$)	–	–	–
HSG	$9.9{\cdot}10^{-7}$ ($\pm8{\cdot}10^{-8}$)	0.71 ($\pm$0.02)	$5.7{\cdot}10^{6}$ ($\pm8{\cdot}10^{5}$)	$4.4{\cdot}10^{-7}$ ($\pm8{\cdot}10^{-8}$)	0.81 ($\pm$0.01)	$2.8{\cdot}10^{4}$ ($\pm2{\cdot}10^{3}$)	$1.5{\cdot}10^{-7}$ ($\pm4{\cdot}10^{-8}$)	0.77 ($\pm$0.01)	$7.0{\cdot}10^{3}$ ($\pm1{\cdot}10^{2}$)
HSG-Ce	$1.2{\cdot}10^{-7}$ ($\pm7{\cdot}10^{-8}$)	0.70 ($\pm$0.01)	$8.0{\cdot}10^{7}$ ($\pm1{\cdot}10^{6}$)	$3.1{\cdot}10^{-8}$ ($\pm5{\cdot}10^{-9}$)	0.83 ($\pm$0.04)	$8.3{\cdot}10^{4}$ ($\pm1{\cdot}10^{3}$)	$1.6{\cdot}10^{-8}$ ($\pm6{\cdot}10^{-9}$)	0.90 ($\pm$0.03)	$3.0{\cdot}10^{3}$ ($\pm1{\cdot}10^{2}$)

+ Units: CPE: F $s^{(n-1)}{\cdot}cm^{-2}$; R: Ω cm^{2}.

(i) The inner layer of the PEO coating (CPE-b/R_b (1 h) and CPE-dl/R_{ct} (21d)): CPE/R-1.
(ii) The outer layer of the PEO coating (CPE-p/R_p (1 h) and CPE-ox/R_{ox} (21d)): CPE/R-2.
(iii) The external HSG coating layer (CPE-HSG/RHSG): CPE/R-3.

For a short immersion time (1 h), the resistance and CPE values of the outer (CPE2/R2) and inner (CPE1/R1) layers of the PEO coating are comparable to those of the HSG coating (CPE3/R3) (Table 5). This may be associated with the relatively low porosity of the PEO coating (Fig. 4), thereby delaying the electrolyte penetration through the coating layers at the early stages of the corrosion process.

For longer immersion times (21 d), the PEO and HSG coatings show an overall decrease in the resistance values of all coating layers and an increase in the CPE values (Table 5). This is associated with the loss of protective barrier properties and the onset of electrochemical activities at the substrate/coating interface [22,46]. This is common for PEO coatings, where the long-term corrosion resistance is usually compromised [7,31].

By contrast, such a decrease is not so evident for HSG-Ce coating, as the resistance values are in the same order of magnitude after 1 h of immersion (Table 5). Considering the comparable thickness between HSG and HSG-Ce coatings, the beneficial effect of Ce incorporation into the HSG-Ce coatings in the long-term corrosion resistance is probably due to the synergic effect of (i) the low porosity of the PEO coating and (ii) improved HSG barrier effect due to a protection mechanism involving the precipitation of Ce compounds. This combined effect may hamper the electrolyte penetration throughout the coating, thus providing the highest long-term corrosion protection [27,47].

After the EIS test, all studied coatings were further analyzed by SEM (Fig. 10) and EDS analysis (Table 6).

As can be seen in Fig. 10a, the PEO coating shows signs of hydration, with most of the pores sealed. Note that the hydration phenomenon was not extensive as the Al/O ratio (0.65; Table 6) is similar to the original surface (0.66; Table 2).

This may be associated to some extent with the formation of aluminium hydroxides as corrosion products, possibly bayerite (β-Al$(OH)_3$) [48]. Besides, its low density compared to γ-Al_2O_3 (~ 2.5 vs. ~ 3.6 g cm^{-3}) can lead to coating cracking due to induced stresses, thus eventually decreasing the overall long-term corrosion protection, as shown in the EIS test (Fig. 8b).

Regarding the HSG and HSG-Ce coatings, the underlying PEO layer was visible due to the HSG cracking. This is possibly related to the HSG layer hydration during the immersion test, thus leading to the hydrolysis of Si-O-Si bonds [22,49] (Figs. 10b, c).

Table 6
EDS analysis (at.%) of PEO, HSG, and HSG-Ce coatings after 21 days of immersion in 3.5 wt% NaCl aqueous solution. Locations are denoted on the top-view SEM micrographs in Fig. 10.

Coating	Location	O	Al	Si	Na	C	Cu	Ce
PEO	1	52.6	34.4	0.9	–	11.1	1.0	–
	1	45.0	17.8	8.0	–	29.0	0.2	–
HSG	2	47.7	35.1	1.3	–	15.4	0.5	–
	3	41.7	11.1	13.1	–	33.9	0.2	–
	1	44.2	11.5	11.5	0.5	31.9	0.2	0.2
HSG-Ce	2	16.9	68.1	12.4	–	–	2.6	–
	3	41.8	2.9	15.1	0.5	39.4	–	0.3

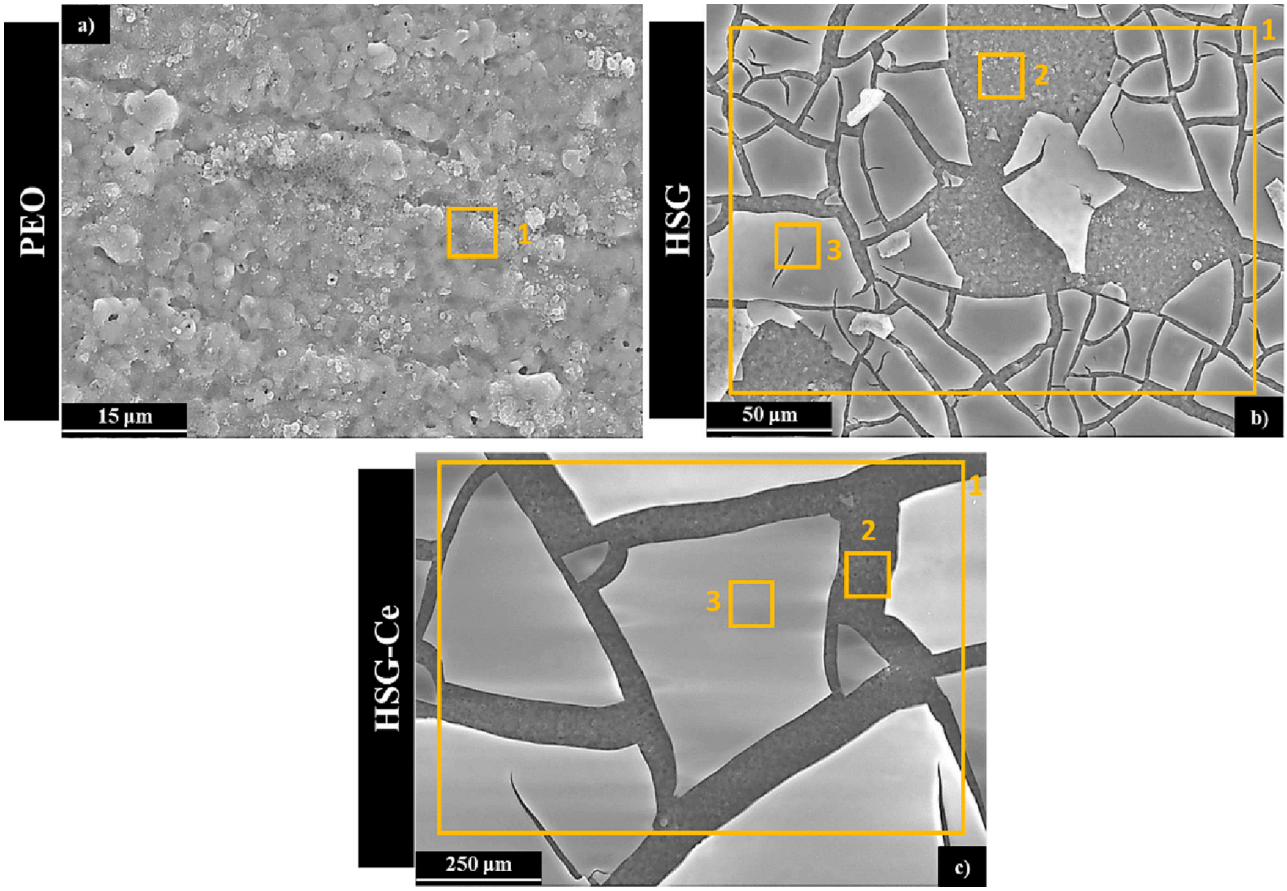

Fig. 10. Top-view scanning electron micrographs of (a) PEO, (b) HSG, and (c) HSG-Ce coatings after 21 days of immersion in 3.5 wt% NaCl aqueous solution. EDS analysis results of the yellow boxed areas are presented in Table 6. (For interpretation of the references to colour in this figure legend, the reader is referred to the web version of this article.)

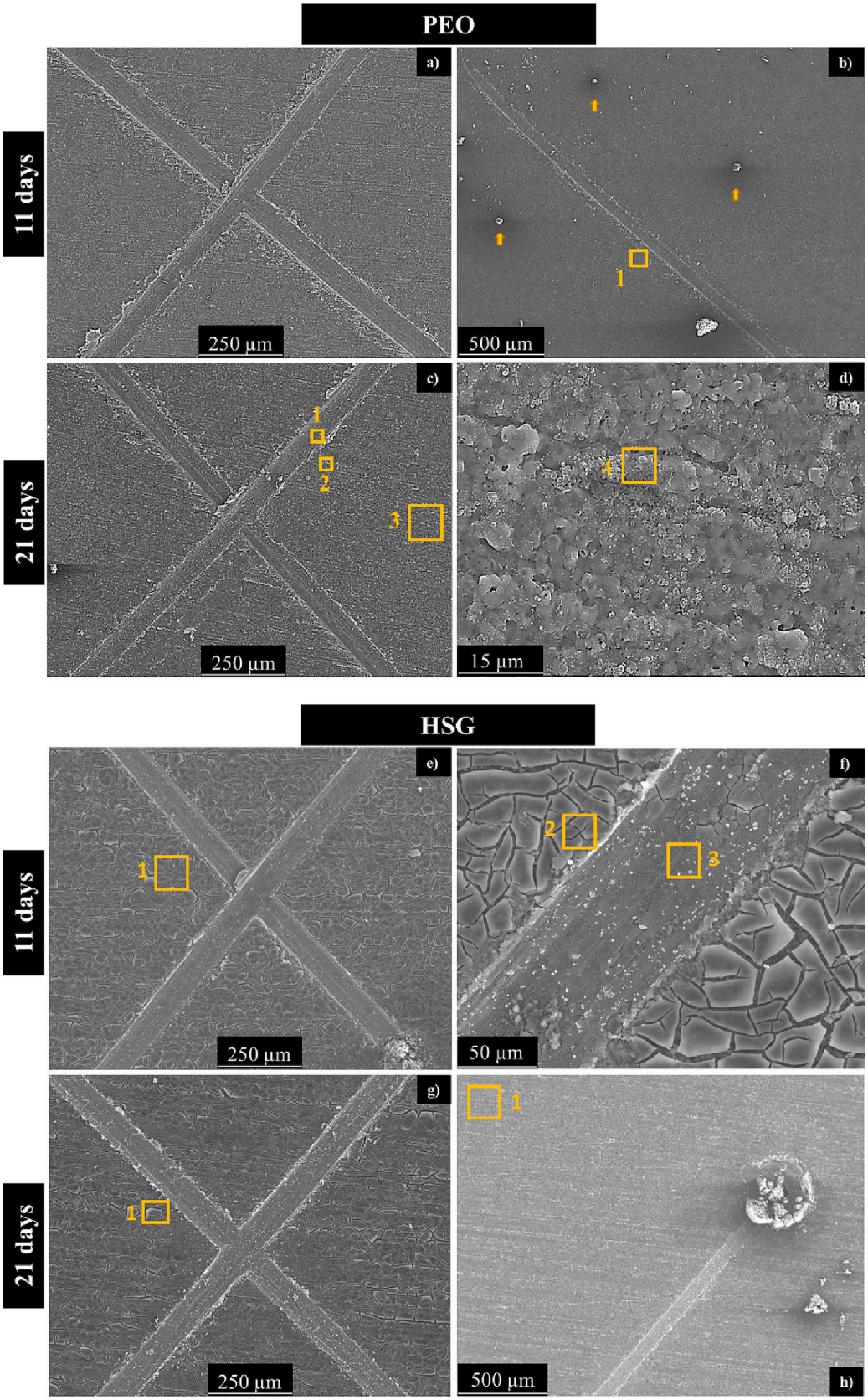

Fig. 11. Scanning electron micrographs corresponding to the scribed plan views of studied coatings after 11 and 21 days immersion in 3.5 wt% NaCl solution. EDS analysis results of the yellow boxed areas are presented in Table 7. (For interpretation of the references to colour in this figure legend, the reader is referred to the web version of this article.)

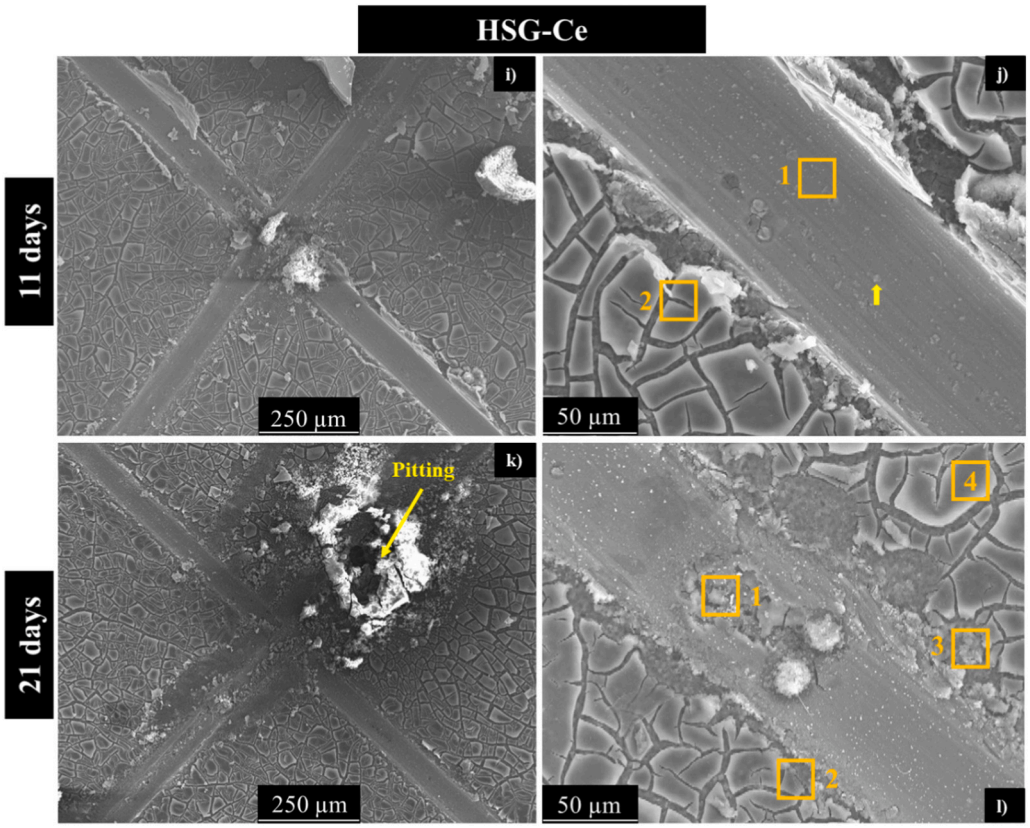

Fig. 11. (*continued*).

This was likewise confirmed by the EDS analysis, where the Si/Al ratio decreases due to a greater contribution from the inner PEO layer (Table 6).

On that basis, the low phase angle values and the non-ideal behaviour of these coatings at the early stages of the corrosion test may be related to the diffusion processes for PEO, HSG, and HSG-Ce coatings. Therefore, the partial HSG layer detachment and the possible protective character of the underneath PEO layer corrosion products may explain the higher impedance and phase angle values for HSG and HSG-Ce coatings after the corrosion test (Fig. 8b, d). Notwithstanding, there is no damage to the underlying AA2024-T3 substrate (Fig. 10).

It is interesting to note that the effect of Ce incorporation is not noticeable from a coating stability point of view. This is opposite to the results found for a Ce-doped HSG coating on conventional anodizing, where a less-cracked surface was observed after the corrosion test for 21 days in 0.1 M NaCl (aq.) [22]. Considering the corrosive character of the chloride anions, the degradation of the inner Flash-PEO layer at the early stages of the corrosion test may also favour the outermost HSG layer detachment.

3.4. Evaluation of active corrosion protection of HSG-coated specimens

Fig. 11 shows the SEM micrographs of the corrosion damage as a function of immersion time on scribed PEO, HSG, and HSG-Ce coatings

Table 7
EDS analysis (at.%) of PEO, HSG, and HSG-Ce scribed coatings after 11 and 21 days immersion in 3.5 wt% NaCl aqueous solution. Locations are denoted on the top-view SEM micrographs in Fig. 10.

Coating	Location	O	Al	Si	Na	C	Cu	Mg	Ce
11 days									
PEO	1	52.4	29.1	2.4	1.2	13.9	1.0	–	
HSG	1	44.7	15.7	8.6	1	29.6	0.4		
	2	46.1	10.8	10.3	1.3	31.1	0.4		
	3	47.7	27.1	5.8	3.6	14.6	1.2		
HSG-Ce	1	9.6	72.4	1.9	–	–	15.8		0.3
	2	41.4	12.8	13.3	1.0	30.4	0.7		0.4
21 days									
PEO	1	52.4	29.1	2.4	1.2	13.9	1.0	–	
	2	53.3	25.9	2.5	1.0	15.2	1.8	0.3	
	3	50.0	28.2	2.5	0.8	15.2	2.9	0.4	
	4	53.7	30.4	1.8	0.2	12.5	1.0	0.4	
HSG	1	46.1	16.1	8.1	1.1	28.2	0.4		
HSG-Ce	1	44.3	23.6	5.3	3.9	20.2	2.7		–
	2	52.0	15.9	9.2	1.5	20.7	0.3		0.4
	3	56.1	25.6	2.4	1.3	13.2	1.2		0.2
	4	44.0	16.5	10.0	0.9	28.4	–		0.2

up to 21 days of immersion in 3.5 wt% NaCl solution. Table 7 shows the corresponding EDS analyses. Note that the selected immersion times in Fig. 11 were those in which visible corrosion was observed (Fig. S3).

After 11 days of immersion, the PEO coating shows the accumulation of corrosion products, possibly related to localized corrosion phenomena (marked with arrows in Fig. 11b). This is in line with the long-term EIS tests (Fig. 8b).

After 21 days of immersion, the high oxygen content on the artificial defect may be related to the formation of aluminium hydroxides (marked as 1 in Fig. 11c). Interestingly, Si (~2.5 at.%) is also detected in this area. This may be associated with the Si release from the PEO coating since the Si content from the AA2024-T3 is negligible (< 0.5 wt % Si; Section 2.1).

In the case of the HSG coating, the sol-gel layer cracking occurs after 11 days of immersion due to water uptake and hydrolysis of the Si-O-Si bonds (Fig. 11b). This cracking is more noticeable in the regions surrounding the scribe due to the induced stresses by the cutting tool. As in the PEO coating, Si was detected in the corrosion products on the scribed surface. Nevertheless, the Si content is higher (~6 at.%; marked as 3 in Fig. 11f) than PEO. This may be due to the additional Si source from the HSG coating.

By contrast, HSG-Ce coating shows a less-cracked surface after 11 and 21 days of immersion. This may be due to the enhanced interaction of HSG-Ce coating with the PEO layer before the corrosion tests (Fig. 4 e, f).

After 11 days of immersion, there are (i) partially corroded areas (~ 9 at.% O; marked as 1 in Fig. 11j), (ii) pitting corrosion, and (iii) corrosion products precipitation with a small amount of Ce (~0.3 at.% Ce, marked as 1 in Fig. 11j).

After 21 days of immersion, the scribed defect surface remains almost unchanged, but the pitting corrosion is more evident (Fig. 11k). The EDS analysis over the pitting surface reveals that the Si signal increases (~5 at.% Si; marked as 1 in Fig. 11l) compared to that observed after 11 days (~2 at.% Si; marked as 1 in Fig. 11j). Regarding Ce distribution, it is worth mentioning that although no Ce was detected in the marked pitting, the cross-section analysis of the HSG-Ce coating after 18 days of immersion (Fig. S4; Table S1) reveals its homogeneous distribution (~0.05–0.08 at.% Ce) over the artificial defect.

Therefore, based on the present findings in SEM/EDS analysis of scribed specimens, a corrosion protection mechanism can be proposed for the HSG-Ce coating.

According to this, when bare Al in the artificial scribe is exposed to the corrosive medium (3.5 wt% NaCl, pH ~6.5), there is a release of Al^{3+} ions (Eq. (1)) and subsequent precipitation of bayerite (Eq. (2)) [22,48].

$$Al(s) \rightarrow Al^{3+}(aq) + 3e^- \quad (1)$$

$$Al^{3+}(aq) + 3H_2O(l) \rightarrow Al(OH)_3(s) + 3H^+(aq) \quad (2)$$

Simultaneously, the gradual PEO coating degradation may result in Si release as silicic acid ($Si(OH)_4$). In the case of HSG-coated PEO coatings, the Si release is higher due to the additional HSG layer contribution. At the studied pH, silicic acid tends to condense and precipitate as amorphous silica particles [50] or even interact with $Al(OH)_3$, leading to the precipitation of amorphous aluminosilicates, which may act as a protective barrier (Eq. (3)) [51,52].

$$Al(OH)_3(s) + Si(OH)_4(aq) \rightarrow (HO)_2Al - O - Si(OH)_3(s) + H_2O(l) \quad (3)$$

Although this mechanism may be common for both HSG coatings, it should be noted that HSG-Ce coating shows a higher susceptibility to pitting corrosion (Fig. 11k). This may be related to the presence of Ce $(NO_3)_3$ in the HSG formulation as explained below.

The presence of Ce (Table 7) is prone to protect where reduction of oxygen takes place (cathodic reaction), i.e., on the intermetallic compounds (IMCs) (Eq. (4)). This reaction increases the local pH at the IMC and promotes the precipitation of $Ce(OH)_3$ (Eq. (5)) and $Ce(OH)_4$ (Eq. (6)). The formation of these hydroxides has been previously reported in a neutral environment at pH above 6, although may also occur at pH ~ 3 when there is Ce^{4+} [22,53].

$$O_2(aq) + 2H_2O(aq) + 4e^- \rightarrow 4OH^-(aq) \quad (4)$$

$$Ce^{3+}(aq) + 3OH^-(aq) \rightarrow Ce(OH)_3(s) \quad (5)$$

$$Ce^{4+}(aq) + 4OH^-(aq) \rightarrow Ce(OH)_4(s) \quad (6)$$

Although the incorporated $Ce(NO_3)_3$ in the sol-gel layer reduces the overall corrosion over the scribed surface, due to Ce release and precipitation of Ce hydroxides, it also appears to induce pitting. This is possibly related to the release of NO_3^- ions.

Nitrate ions are efficient inhibitors for aluminium as they favour the formation of protective oxide films over the aluminium alloy matrix. However, in competition, preferential dissolution of Cu-rich particles may occur in presence of nitrate ions, the cathodic reaction being the reduction of nitrate ions [54].

In the present study, it is worth mentioning that N was not detected by EDS analysis of the HSG-Ce coating (Table 7). A possible explanation for this finding may be its incorporation in the inner HSG coating part at a minimal concentration.

Therefore, it is possible that NO_3^- release, even at minimal concentrations, may be responsible for promoting pitting corrosion phenomena at the IMC regions instead of forming a thick and stable NO_3^--rich passive layer (Fig. 11 k, i). Based on the results by Blanc et al. [54], it is suggested that a higher liberation of NO_3^- is needed to further enhance the stability of the passive film and minimize pitting in the scribed area. Hereto, present findings indicate that the active protection mechanism of HSG-Ce coating may be associated mainly with both Si and Ce species.

4. Conclusions

The main conclusions regarding the synthesis, characterization, and corrosion performance of the studied inhibitor-free and Ce-containing Flash PEO-HSG coatings can be summarized as follows:

- PEO coatings with an energy consumption of ~5.3 kW h m^{-2} μm^{-1} and ~2.5 μm thickness were successfully produced on a 2024-T3 aluminium alloy by using a silicate-phosphate-based electrolyte. The energy consumption and thickness values for the studied PEO coating are considerably lower compared to conventional PEO treatments on Al alloys. The coating revealed submicrometric pores and was mainly composed of γ-Al_2O_3 with traces of Si and P.
- Hybrid sol-gel sealings based on TEOS and GPTMS precursors produced a uniform crack-free 4 μm-thick top layers with lower roughness in comparison to the PEO coating. Trace amounts of Ce (~0.2 %) were successfully incorporated into the sol-gel sealing by using $Ce(NO_3)_3$ in the precursor solution. Ce was heterogeneously distributed across the thickness of the sealing layer.
- FTIR results revealed the successful development of the sol-gel coatings. The presence of Ce seemed to promote the cross-linking of the organic part in the GPTMS precursor. Both inhibitor-free and inhibitor-containing sol-gel sealings revealed excellent adhesion to the base PEO coating. Contact angle measurements showed the hydrophilic character of the PEO coating and the hydrophobic nature of the sealed systems.
- All the investigated coating systems improve the corrosion behaviour of the 2024-T3 alloy in a saline medium by up to 3 to 4 orders of magnitude. Electrochemical tests indicated that the HSG-Ce coating revealed the best corrosion performance after 21 days of immersion in 3.5 wt% NaCl.
- Specimens with an artificial scribe showed an acceptable corrosion performance after 21 days of immersion in 3.5 wt% NaCl. The unsealed PEO coating revealed signs of hydration and pitting, but the

scribe remained largely unaffected with only a slight formation of corrosion products. The latter revealed Si which was released from the surrounding coating. HSG sealing showed degradation in the form of cracking but remained attached to the surface. The scribe in the inhibitor-free formulation revealed significant amounts of Si (~5 %), indicating an active protection mechanism involving the precipitation of aluminosilicates. The Ce-containing sealing revealed a similar behaviour, however, it is suggested that NO_3^- release promoted localized corrosion phenomena in the scribe.

Present findings reveal that HSG-Ce coating will be considered a promising alternative to hexavalent chromium-free systems for non-painted components in the aircraft industry. Nevertheless, more studies concerning localized electrochemical tools, mechanical performance, and up-scaling should be carried out in the future to meet the stringent requirements in the aircraft industry.

CRediT authorship contribution statement

R. del Olmo: Conceptualization, Data curation, Formal analysis, Investigation, Methodology, Writing – original draft, Writing – review & editing. **E. López:** Conceptualization, Data curation, Formal analysis, Investigation, Methodology, Writing – original draft, Writing – review & editing. **E. Matykina:** Conceptualization, Formal analysis, Funding acquisition, Project administration, Resources, Supervision, Validation, Writing – review & editing. **U. Tiringer:** Data curation, Methodology, Writing – review & editing. **J.M.C. Mol:** Formal analysis, Resources, Validation, Writing – review & editing. **M. Mohedano:** Conceptualization, Formal analysis, Funding acquisition, Project administration, Resources, Supervision, Validation, Writing – review & editing. **R. Arrabal:** Conceptualization, Formal analysis, Funding acquisition, Project administration, Resources, Supervision, Validation, Writing – review & editing.

Declaration of competing interest

The authors declare that they have no known competing financial interests or personal relationships that could have appeared to influence the work reported in this paper.

Data availability

The raw/processed data required to reproduce these findings cannot be shared at this time as the data also forms part of an ongoing study.

Acknowledgments

The authors gratefully acknowledge the support of the PID2021-124341OB-C22 (MCINN/AEI/FEDER, UE), ADITIMAT-CM (S2018/NMT/4411, Regional Government of Madrid and EU Structural and Social funds). M. Mohedano is grateful for the support of RYC-2017 21843. R. del Olmo acknowledges the financial support from the *Margarita Salas* CT18/22 postdoctoral grant.

Appendix A. Supplementary data

Supplementary data to this article can be found online at https://doi.org/10.1016/j.porgcoat.2023.107667.

References

[1] P. Visser, H. Terryn, J.M.C. Mol, Aerospace coatings, in: Springer Series in Materials Science, 2016, pp. 315–372.
[2] S.T. Abrahami, J.M.M. de Kok, H. Terryn, J.M.C. Mol, Towards Cr(VI)-free anodization of aluminum alloys for aerospace adhesive bonding applications: a review, Front. Chem. Sci. Eng. 11 (2017) 465–482.
[3] H.G. International, Use of Potassium Dichromate for Sealing After Anodizing Applications by Aerospace Companies and Their Suppliers, Available from, https://echa.europa.eu/documents/10162/d6c88cd1-ef18-460b-8493-e1d59211a888, 2018, p. 65.
[4] LANXESS, Surface treatment for applications in the aeronautics and aerospace industries, in: Analysis of Alternatives, Non-confidential Report, 2018, p. 137. Available from, https://echa.europa.eu/es/support/substance-identification.
[5] M. Mohedano, X. Lu, E. Matykina, C. Blawert, R. Arrabal, M.L. Zheludkevich, Plasma electrolytic oxidation (PEO) of metals and alloys, in: Encyclopedia of Interfacial Chemistry, Surface Science and Electrochemistry, 2018, pp. 423–438.
[6] E. Matykina, R. Arrabal, M. Mohedano, B. Mingo, J. Gonzalez, A. Pardo, M. C. Merino, Recent advances in energy efficient PEO processing of aluminium alloys, in: Transactions of Nonferrous Metals Society of China (English Edition) 27, 2017, pp. 1439–1454.
[7] R. del Olmo, M. Mohedano, P. Visser, E. Matykina, R. Arrabal, Flash-PEO coatings loaded with corrosion inhibitors on AA2024, Surf. Coat. Technol. 402 (2020).
[8] R. del Olmo, M. Mohedano, B. Mingo, R. Arrabal, E. Matykina, LDH post-treatment of flash PEO coatings, Coatings 9 (2019).
[9] L. Wen, Y. Wang, Y. Zhou, J.-H. Ouyang, L. Guo, D. Jia, Corrosion evaluation of microarc oxidation coatings formed on 2024 aluminium alloy, Corros. Sci. 52 (2010) 2687–2696.
[10] Y. Cao, D. Zheng, F. Zhang, J. Pan, C. Lin, Layered double hydroxide (LDH) for multi-functionalized corrosion protection of metals: a review, J. Mater. Sci. Technol. 102 (2022) 232–263.
[11] M. Kaseem, S. Fatimah, N. Nashrah, Y.G. Ko, Recent progress in surface modification of metals coated by plasma electrolytic oxidation: principle, structure, and performance, Prog. Mater. Sci. 117 (2021), 100735.
[12] S. Zheng, J. Li, Inorganic–organic sol gel hybrid coatings for corrosion protection of metals, J. Sol-Gel Sci. Technol. 54 (2010) 174–187.
[13] R.B. Figueira, C.J.R. Silva, E.V. Pereira, Organic–inorganic hybrid sol–gel coatings for metal corrosion protection: a review of recent progress, J. Coat. Technol. Res. 12 (2015) 1–35.
[14] R.B. Figueira, I.R. Fontinha, C.J.R. Silva, E.V. Pereira, Hybrid sol-gel coatings: smart and green materials for corrosion mitigation, in: Coatings, 2016.
[15] C.J. Brinker, G.W. Scherer, CHAPTER 10 - surface chemistry and chemical modification, in: C.J. Brinker, G.W. Scherer (Eds.), Sol-gel Science, Academic Press, San Diego, 1990, pp. 616–672.
[16] H. Costenaro, A. Lanzutti, Y. Paint, L. Fedrizzi, M. Terada, H.G. de Melo, M. G. Olivier, Corrosion resistance of 2524 Al alloy anodized in tartaric-sulphuric acid at different voltages and protected with a TEOS-GPTMS hybrid sol-gel coating, Surf. Coat. Technol. 324 (2017) 438–450.
[17] M. Terada, F.M. Queiroz, D.B.S. Aguiar, V.H. Ayusso, H. Costenaro, M.G. Olivier, H.G. de Melo, I. Costa, Corrosion resistance of tartaric-sulfuric acid anodized AA2024-T3 sealed with Ce and protected with hybrid sol–gel coating, Surf. Coat. Technol. 372 (2019) 422–426.
[18] T.T. Thai, M.E. Druart, Y. Paint, A.T. Trinh, M.G. Olivier, Influence of the sol-gel mesoporosity on the corrosion protection given by an epoxy primer applied on aluminum alloy 2024 –T3, Prog. Org. Coat. 121 (2018) 53–63.
[19] U. Tiringer, B. Mušič, D. Zimerl, G. Šekularac, S. Stavber, I. Milošev, The effects of cerium ions on the curing, polymerisation and condensation of hybrid sol-gel coatings, J. Non-Cryst. Solids 510 (2019) 93–100.
[20] M. Whelan, E. Tobin, J. Cassidy, B. Duffy, Optimization of anodic oxidation of aluminum for enhanced adhesion and corrosion properties of sol-gel coatings, J. Electrochem. Soc. 163 (2016) C205–C212.
[21] K.A. Yasakau, S. Kallip, M.L. Zheludkevich, M.G.S. Ferreira, Active corrosion protection of AA2024 by sol-gel coatings with cerium molybdate nanowires, Electrochim. Acta 112 (2013) 236–246.
[22] R. del Olmo, U. Tiringer, I. Milošev, P. Visser, R. Arrabal, E. Matykina, J.M.C. Mol, Hybrid sol-gel coatings applied on anodized AA2024-T3 for active corrosion protection, Surf. Coat. Technol. 419 (2021).
[23] U. Tiringer, A. Durán, Y. Castro, I. Milošev, Self-healing effect of hybrid sol-gel coatings based on GPTMS, TEOS, SiO2 nanoparticles and Ce(NO3)3 applied on aluminum alloy 7075-T6, J. Electrochem. Soc. 165 (2018) C213–C225.
[24] I. Recloux, M. Debliquy, A. Baroni, Y. Paint, A. Lanzutti, L. Fedrizzi, M.-G. Olivier, Optimization of synthesis parameters of mesoporous silica sol–gel thin films for application on 2024 aluminum alloy substrates, Appl. Surf. Sci. 277 (2013) 201–210.
[25] L. Sopchenski, J. Robert, M. Touzin, A. Tricoteaux, M.-G. Olivier, Improvement of wear and corrosion protection of PEO on AA2024 via sol-gel sealing, Surf. Coat. Technol. 417 (2021), 127195.
[26] D. Balgude, A. Sabnis, Sol–gel derived hybrid coatings as an environment friendly surface treatment for corrosion protection of metals and their alloys, J. Sol-Gel Sci. Technol. 64 (2012) 124–134.
[27] U. Tiringer, I. Milošev, A. Durán, Y. Castro, Hybrid sol–gel coatings based on GPTMS/TEOS containing colloidal SiO2 and cerium nitrate for increasing corrosion protection of aluminium alloy 7075-T6, J. Sol-Gel Sci. Technol. 85 (2018) 546–557.
[28] L.G. Ecco, M. Fedel, F. Deflorian, J. Becker, B.B. Iversen, A. Mamakhel, Waterborne acrylic paint system based on nanoceria for corrosion protection of steel, Prog. Org. Coat. 96 (2016) 19–25.
[29] E. Matykina, R. Arrabal, A. Pardo, M. Mohedano, B. Mingo, I. Rodríguez, J. González, Energy-efficient PEO process of aluminium alloys, Mater. Lett. 127 (2014) 13–16.
[30] L. Guo-Hua, G. Wei-Chao, C. Huan, L. Li, N. Er-Wu, Y. Si-Ze, Microstructure and corrosion performance of oxide coatings on aluminium by plasma electrolytic

oxidation in silicate and phosphate electrolytes, Chin. Phys. Lett. 23 (2006) 3331–3333.
[31] G. Wei-Chao, L. Guo-Hua, C. Huan, C. Guang-Liang, F. Wen-Ran, Z. Gu-Ling, Y. Si-Ze, Investigation of morphology and composition of plasma electrolytic oxidation coatings in systems of Na2SiO3–NaOH and (NaPO3)6–NaOH, J. Mater. Process. Technol. 182 (2007) 28–33.
[32] W. Yang, B.-l. Jiang, H.-y. Shi, L.-y. Xian, Effects of KMnO4 on microstructure and corrosion resistance of microarc oxidation coatings on 2024 aluminum alloy, J. Cent. S. Univ. Technol. 17 (2010) 223–227.
[33] L. Zhu, Z. Guo, Y. Zhang, Z. Li, M. Sui, A mechanism for the growth of a plasma electrolytic oxide coating on Al, Electrochim. Acta 208 (2016) 296–303.
[34] J.-B. Cambon, J. Esteban, F. Ansart, J.-P. Bonino, V. Turq, S.H. Santagneli, C. V. Santilli, S.H. Pulcinelli, Effect of cerium on structure modifications of a hybrid sol–gel coating, its mechanical properties and anti-corrosion behavior, Mater. Res. Bull. 47 (2012) 3170–3176.
[35] U. Tiringer, J.P.B. van Dam, S.T. Abrahami, H. Terryn, J. Kovač, I. Milošev, J.M. C. Mol, Scrutinizing the importance of surface chemistry versus surface roughness for aluminium / sol-gel film adhesion, Surf. Interf. 26 (2021), 101417.
[36] A. Trentin, S.V. Harb, M.C. Uvida, S.H. Pulcinelli, C.V. Santilli, K. Marcoen, S. Pletincx, H. Terryn, T. Hauffman, P. Hammer, Dual role of lithium on the structure and self-healing ability of PMMA-silica coatings on AA7075 alloy, ACS Appl. Mater. Interfaces 11 (2019) 40629–40641.
[37] N.L. Sukiman, X. Zhou, N. Birbilis, A.E. Hughes, J.M.C. Mol, S.J. Garcia, X. Zhou, G.E. Thompson, Durability and corrosion of aluminium and its alloys: overview, property space, techniques and developments, in: A. Zaki (Ed.), Aluminium Alloys, IntechOpen, Rijeka, 2012 (pp. Ch. 2).
[38] W.T. Al-Rubayee, O.F. Abdul-Rasheed, N.M. Ali, Preparation of a modified nanoalumina sorbent for the removal of alizarin yellow R and methylene blue dyes from aqueous solutions, J. Chem. 2016 (2016) 4683859.
[39] V. Dalmoro, J.H.Z. dos Santos, C. Alemán, D.S. Azambuja, An assessment of the corrosion protection of AA2024-T3 treated with vinyltrimethoxysilane/(3-glycidyloxypropyl)trimethoxysilane, Corros. Sci. 92 (2015) 200–208.
[40] H. Pérez, R. Miranda, Z. Saavedra-Leos, R. Zarraga, P. Alonso, E. Moctezuma, J. Martínez, Green and facile sol–gel synthesis of the mesoporous SiO2–TiO2 catalyst by four different activation modes, RSC Adv. 10 (2020) 39580–39588.
[41] C.A. Hernández-Barrios, J.A. Saavedra, S.L. Higuera, A.E. Coy, F. Viejo, Effect of cerium on the physicochemical and anticorrosive features of TEOS-GPTMS sol-gel coatings deposited on the AZ31 magnesium alloy, Surf. Interf. 21 (2020), 100671.
[42] R.K. Suleiman, A.Y. Adesina, A.M. Kumar, M.M. Rahman, F.A. Al-Badour, B. El Ali, Anticorrosion properties of a novel hybrid sol-gel coating on aluminum 3003 alloy, Polymers 14 (2022).
[43] T.T. Thai, A.T. Trinh, M.-G. Olivier, Hybrid sol–gel coatings doped with cerium nanocontainers for active corrosion protection of AA2024, Prog. Org. Coat. 138 (2020), 105428.
[44] Y. Castro, E. Özmen, A. Durán, Integrated self-healing coating system for outstanding corrosion protection of AA2024, Surf. Coat. Technol. 387 (2020), 125521.
[45] P. Visser, A. Lutz, J.M.C. Mol, H. Terryn, Study of the formation of a protective layer in a defect from lithium-leaching organic coatings, Prog. Org. Coat. 99 (2016) 80–90.
[46] R.V. Lakshmi, S.T. Aruna, C. Anandan, P. Bera, S. Sampath, EIS and XPS studies on the self-healing properties of Ce-modified silica-alumina hybrid coatings: evidence for Ce(III) migration, Surf. Coat. Technol. 309 (2017) 363–370.
[47] K. Czelej, M.R. Zemła, P. Śpiewak, T. Wejrzanowski, K.J. Kurzydłowski, Atomic-scale computational design of hydrophobic RE surface-doped Al2O3 and TiO2, Phys. Chem. Chem. Phys. 19 (2017) 21119–21126.
[48] G. Lefèvre, M. Duc, P. Lepeut, R. Caplain, M. Fédoroff, Hydration of γ-alumina in water and its effects on surface reactivity, Langmuir 18 (2002) 7530–7537.
[49] M. Hernández-Escolano, M. Juan-Díaz, M. Martínez-Ibáñez, A. Jimenez-Morales, I. Goñi, M. Gurruchaga, J. Suay, The design and characterisation of sol–gel coatings for the controlled-release of active molecules, J. Sol-Gel Sci. Technol. 64 (2012) 442–451.
[50] M.J. Juan-Díaz, M. Martínez-Ibáñez, M. Hernández-Escolano, L. Cabedo, R. Izquierdo, J. Suay, M. Gurruchaga, I. Goñi, Study of the degradation of hybrid sol–gel coatings in aqueous medium, Prog. Org. Coat. 77 (2014) 1799–1806.
[51] J. Beardmore, X. Lopez, J.I. Mujika, C. Exley, What is the mechanism of formation of hydroxyaluminosilicates? Sci. Rep. 6 (2016) 30913.
[52] V. Abbas, M. Malki, Aluminum Silicate Formation in Membrane Separation Processes: Facts vs. Myths, AMTA/AWWA Membrane Technology Conference and Exposition 2013, 2013, pp. 1071–1091.
[53] K.A. Yasakau, M.L. Zheludkevich, S.V. Lamaka, M.G.S. Ferreira, Mechanism of corrosion inhibition of AA2024 by rare-earth compounds, J. Phys. Chem. B 110 (2006) 5515–5528.
[54] C. Blanc, S. Gastaud, G. Mankowski, Mechanistic studies of the corrosion of 2024 aluminum alloy in nitrate solutions, J. Electrochem. Soc. 150 (2003) B396.